Non-affine deformation in microstructure selection in solids II: Elastoplastic theory for the dynamics of solid state transformations

Non-affine deformation in microstructure selection in solids II: Elastoplastic theory for the dynamics of solid state transformations

Arya Paul[1], Jayee Bhattacharya[1], Surajit Sengupta[1] and Madan Rao[2,3]

[1] S N Bose National Centre for Basic Sciences, Block JD, Sector III, Salt Lake, Calcutta 700 098, India
[2] Raman Research Institute, C V Raman Avenue, Bangalore 560 080, India
[3] National Centre for Biological Sciences (TIFR), Bellary Road, Bangalore 560 065, India

Abstract
We study the nucleation dynamics of a model solid state transformation and the criterion for microstructure selection. Using a molecular dynamics (MD) simulation, we had shown that the dynamics of the solid is accompanied by the creation of transient *non-affine zones* (NAZ), which evolve with the rapidly moving transformation front. Guided by our MD results, we formulate a dynamical continuum theory of solid state transformation, which couples the elastic strain to the non-affine deformation. We demonstrate that our *elastoplastic* description recovers all qualitative features of the MD simulation. We construct a dynamical phase diagram for microstructure selection, including regimes where martensite or ferrite obtains, in addition to making several testable predictions.

(Some figures in this article are in colour only in the electronic version)

1. Introduction

The dynamics following a quench across a solid state structural transition results in a variety of microstructures depending on the rate and depth of quench. A key question in the physics of solid state nucleation is to understand the dynamical criterion for microstructure selection. In an MD simulation of a model solid [1] (Part I), we motivated and described our search for new dynamical variables, which in addition to the conventional elastic strain fields, would describe the dynamics of solids following a quench. The new dynamical variables, identified as non-affine zones (NAZ), were shown to be generated by the nucleation process; their fast dynamics governed the final microstructure of the solid. In this part II, we formulate a continuum dynamical theory of microstructure selection based on the coupling between the non-affine variables and elastic strain.

Our MD simulations of the model solid undergoing a two-dimensional square to rhombic structural transition (Part I) reveal four principles which form the basis for an elastoplastic

theory (section 2). (i) The product solid grows within the parent matrix following heterogeneous nucleation. (ii) The onset of nucleation produces *both* order parameter (OP) strains (shear and deviatoric) and non-order parameter (NOP) strain (volumetric), the latter being *slaved* to the former. (iii) The transformation is accompanied by zones of transient plasticity called non-affine zones (NAZ), whose dynamics determine the microstructure. (iv) NAZs are produced when the local stress exceeds a threshold.

This elastoplastic theory, specialized to the case of the square to rhombus transition (section 3), reproduces the dynamics and patterning of the strain (both OP and NOP) and NAZs in [1]. We exhibit a non-equilibrium phase diagram (section 4) showing the two classes of microstructures, namely, a twinned, anisotropic *martensite* and an untwinned, isotropic *ferrite*, obtained in our MD simulations. In the limit of slow dynamics of plasticity, the elastoplastic description becomes identical to the strain-only theory [2], as long as it is coarse-grained over scales larger than λ, the typical size of the NAZ (section 5).
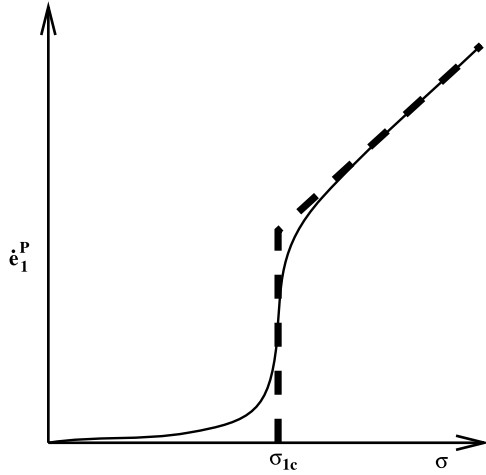
Figure 1. Pictorial representation of the dynamics of the plastic strain e_1^P as a function of the local volumetric stress σ_1 for a typical flowing solid (solid line) and the simplified form (13) used in our computations (dashed line).

2. Elastoplastic theory of solid state nucleation

To describe the solid state transformation with elastic and plastic strains, we first write the total strain tensor as $\epsilon \equiv \{\epsilon_T^A, \epsilon_V\}$, where the affine OP or transformation strain ϵ_T^A connects the parent and product lattices, and the NOP strain ϵ_V is split into an affine part and a non-affine or plastic strain, $\epsilon_V = \epsilon_V^A - \epsilon_V^P$ (we have dropped the tensor indices for clarity). Note that our association of plasticity with the NOP strain *alone* follows from Part I. However, as we remarked, this could be special to the square-to-rhombus transformation. In general, there could be plastic deformations associated with the OP strain too; we will comment on this in section 5.

The transformation is described by a free-energy functional

$$\mathcal{F} = \int_{\mathbf{r}} f_T(\{\epsilon_T^A\}, \{\epsilon_V^A\}, \{\nabla \epsilon_T^A\}, \{\nabla \epsilon_V^A\}) + f_c(\{\epsilon_T^A\}, \{\epsilon_V\}) \quad (1)$$

where the homogeneous part of the free-energy density $f_T(\{\epsilon_T^A\}, \ldots)$ has three minima corresponding to the parent phase $\epsilon_T^A = 0$ and (symmetry-related) variants of the product phase, $\epsilon_T^A \neq 0$. The functional $\mathcal{F}$ is constructed from invariants of the smallest symmetry group containing the symmetries of the parent and product as subgroups, and is in general nonlinear in the strains. In the absence of plastic deformations, a variation of (1) with respect to ϵ_V^A, gives the desired relation connecting the OP and the NOP strain.

The driving force for ϵ_T^A is the chemical potential gradient $\delta \mathcal{F}/\delta \epsilon_T^A$ to form the rhombic phase. The dynamical equations for the order parameter strain, which includes dissipation and inertia, take the general form [2]

$$\Psi(\epsilon_T^A, \dot{\epsilon}_T^A, \ddot{\epsilon}_T^A; \epsilon_V) = 0. \quad (2)$$

The dynamics of the affine NOP strain is slaved to the OP strain. This takes the form of a local force balance [3]:

$$\nabla \cdot \sigma_V = 0 \quad (3)$$

where the local NOP stress σ_V is related to the instantaneous equilibrium value of the NOP strain:

$$\sigma_V = \frac{\partial \mathcal{F}}{\partial \epsilon_V^A}. \quad (4)$$

The dynamical equations for the plastic NOP strain ϵ_V^P are constructed phenomenologically following the principles listed above. We include the physics of threshold stress and yield flow by a constitutive relation between stress and strain rate (see figure 1):

$$\begin{aligned} \dot{\epsilon}_V^P &= \frac{1}{h} f_1(\sigma_V) && \text{if } g(\sigma_V - \sigma_{Vc}) > 0 \\ &= f_2(\sigma_V) && \text{otherwise} \end{aligned} \quad (5)$$

where h and σ_{Vc} are material parameters and $g(\sigma_V; \sigma_{Vc})$ is the appropriate (material-dependent) threshold or yield criterion [4], which in principle can incorporate history dependence and ultimately account for the observed dependence of microstructure on external factors like the quench depth and rate of quench. Within our elastoplastic model this connection may be made either using experimentally fitted parameters, or using quantities obtained from molecular dynamics calculations by a systematic coarse-graining procedure or, finally, derived from a more microscopic non-affine field theory (see, for example, [5]). We hope to carry out the latter program in detail in a future study. In general, the function $f_2(\sigma_V)$ allows for the possibility that the solid exhibits finite 'creep' ($\dot{\epsilon}_V^P \neq 0$ at $\sigma = 0$) (5). In the next section, we will, however, set the creep to zero, as motivated by our MD results, figure 7 of [1], and make the simplified 'Newtonian' ansatz, $f_1(\sigma_V) = \sigma_V$, when $|\sigma_V| > \sigma_{Vc}$. For this case the parameter h is related to the relaxation time of plastic flow. The ratio of the stress to strain rate, $\sigma/\dot{\epsilon}_V^P = \eta$, is a bulk viscosity. At the yield stress, this viscosity diverges, signifying jamming. Note σ is an internal stress and can therefore locally decrease and increase once the solid yields, giving rise to oscillatory behavior, as seen in figure 7 of [1].

Finally, owing to plasticity, the local affine strains do not satisfy the usual St. Venant's compatibility [6]—instead, the amount of incompatibility is *exactly accounted for by the amount of plasticity generated*. This implies that the local St. Venant's condition should be rewritten as [7]

$$\nabla \times (\nabla \times \epsilon)^\dagger = 0 \quad (6)$$

where ϵ is the *total* strain, which includes ϵ_V^P. In regions where the local plastic deformation is zero, this reduces to the usual St. Venant's compatibility condition.

The equations of constraint, (3) and (6), are used to express ϵ_V^A in terms of ϵ_T^A; equations (2) and (5) are then used with appropriate initial conditions to describe the elastoplastic theory for the dynamics of solid state transformations.

To initiate heterogeneous nucleation, one needs to introduce random 'seeds' into the deterministic equations (2) and (5). This is done via initial conditions in the local strain ϵ_T^A or the local stress σ_V. A random initial distribution of the stress σ_V can produce local plastic strain e_V^P, if the local σ_V is larger than the yield stress. This will in turn nucleate the

transformed solid via ϵ_T^A. The results obtained from solving the dynamical equations must then be averaged over realizations of the quenched random stress field. A simpler strategy is to directly introduce a seed in the transformation strain, ϵ_T^A, by creating a small twinned region with a single twin boundary (since the dynamics of ϵ_T^A is conserved). This allows us to follow the subsequent dynamics in precise detail and does not require any averaging over noise realizations.

We use the elastoplastic model to address two separate but related issues. We will first determine the late time *morphology* and *microstructure* of the growing nucleus following a quench across the structural phase boundary and construct a dynamical phase diagram akin to figure 2 of our MD simulation [1] or figure 4 of [8]. We compute the shape of the growing nucleus from the shape asphericity $A = (\lambda_1 - \lambda_2)/(\lambda_1 + \lambda_2)$, where λ_i are the eigenvalues of the moment of inertia tensor of the nucleus [1]. For a circular (*isotropic*) nucleus $\lambda_1 = \lambda_2$ and $A = 0$, while for highly eccentric ellipses $A \to 1$. By quenching into different regions of the dynamical phase diagram, we will study the dynamics by which a specific microstructure gets selected.

3. Elastoplastic theory: square to rhombus transformation

We use the above formalism to describe the specific square to rhombus transformation, so as to be able to make a detailed comparison with the results of our MD simulation. The square to rhombus transformation is a special case of the square ($p4mm$) to oblique ($p2$), and is thus described by two order parameter strains characterizing the 4-degenerate product phases. In general, one can construct a Landau theory for this transition [9] using terms up to sixth order in the OP strains $e_T^A = \{e_2, e_3\}$ and quadratic in the NOP strain $\epsilon_V \equiv e_1$. Here $e_1 = e_{xx} + e_{yy}$, $e_2 = e_{xx} - e_{yy}$ and $e_3 = e_{xy} = e_{yx}$. We then decompose the NOP strain into a slaved, affine NOP strain $\epsilon_V^A \equiv e_1^A$ and a dynamical non-affine NOP strain $\epsilon_V^P \equiv e_1^P$, enabling the total NOP strain to be written as $e_1 = \epsilon_1^A - \epsilon_1^P$.

In order to compare with the results and phenomenology of the MD simulation of the model solid described in [1], we look at a restriction of this problem. Recall that our microscopic potential supports *two* rather than the possible four product minima [1]. This implies that, for this choice of potential, there is therefore only *one* minimum in the e_2 direction; it thus suffices to retain up to quadratic terms in e_2 in the strain free-energy functional. The minimal free-energy functional, sufficient to describe this square to rhombus transition, is given by

$$\mathcal{F} = \tfrac{1}{2} \int \mathrm{d}x\mathrm{d}y [a_1(e_1 + e_1^P)^2 + a_2 e_2^2 + a_3 e_3^2$$
$$+ c_1(\nabla(e_1 + e_1^P))^2 + c_2(\nabla e_2)^2 + (\nabla e_3)^2 - e_3^4 + e_3^6] \quad (7)$$

in terms of the OP strains e_3 and e_2 and the NOP strain e_1. The only other term to quadratic order in e_2, namely $e_2^2 e_3^4$, has been dropped as it does not influence the phase transition. The three elastic constants $a_1 = K_{11} + K_{12}/2$, $a_2 = K_{11} - K_{12}/2$ and $a_3 = 2K_{44}$ define the linear elasticity of the square phase with K_{11}, K_{22} and K_{44} being the conventional elastic constants of a solid with square symmetry [3]. The coefficients of the quartic and sixth-order terms as well as that of ∇e_3 can be scaled to unity by rescaling e_1, $\mathcal{F}$ and the spatial coordinates (x, y). The coefficient a_3 represents the degree of under-cooling; we work in a parameter range where the square crystal is metastable and the rhombic crystal is stable at equilibrium. Finally, note that all the parameters in (7) may, if so desired, be obtained for any particular material by fitting, for example, to standard neutron scattering data [2].

The affine NOP strain is slaved to the OP strains; we make use of the conditions of mechanical equilibrium ($\nabla \cdot \boldsymbol{\sigma} = 0$) and *modified* St. Venant compatibility to express e_1^A in terms of e_2 and e_3:

$$\nabla^2 e_1 - (\nabla_x^2 - \nabla_y^2)e_2 - 4\nabla_x \nabla_y e_3 = 0. \quad (8)$$

The relation between the total NOP strain e_1 and the OP strains e_j, $j = 2, 3$ is most conveniently expressed in **k**-space:

$$\tilde{e}_1(\mathbf{k}) = \tilde{\mathcal{Q}}_{1j}(\mathbf{k})\tilde{e}_j(\mathbf{k}) \quad (9)$$

with the kernels

$$\tilde{\mathcal{Q}}_{13}(\mathbf{k}) = \frac{4a_2 - 2a_3}{a_1 + a_2} \frac{k_x k_y}{k^2}$$
$$= q_{13} \frac{k_x k_y}{k^2}, \quad (10)$$

and

$$\tilde{\mathcal{Q}}_{12}(\mathbf{k}) = -\frac{a_3 - 2a_2}{2a_1 + a_3} \frac{k_x^2 - k_y^2}{k^2}$$
$$= -q_{12} \frac{k_x^2 - k_y^2}{k^2}. \quad (11)$$

In effect, the above equations of constraint connect the instantaneous e_1^A to the dynamical e_1^P, e_2 and e_3.

We now specify the dynamics for the OP strains and the plastic NOP strain. At this stage we make the approximation of replacing the value of the OP e_2 by its value at equilibrium, i.e. $e_2 = 0$, for all times. This greatly simplifies the calculation without changing the physics. The dynamical equation for the affine OP strain e_3 may be derived from Newton's laws [2] incorporating dissipation via a Rayleigh dissipation functional [3]:

$$\frac{\partial^2 e_3}{\partial t^2} = \nabla^2 \left[\frac{\delta \mathcal{F}}{\delta e_3} + \gamma \frac{\partial e_3}{\partial t} \right], \quad (12)$$

where γ is a solid shear viscosity.

The dynamics of the plastic NOP strain are determined by the phenomenological equation:

$$\dot{e}_1^P = \frac{1}{h_1} \sigma_1 \qquad \text{if } |\sigma_1| > \sigma_{1c}$$
$$= 0 \qquad \text{otherwise} \quad (13)$$

where the local stress $\sigma_1 = \delta \mathcal{F}/\delta e_1$ and we have, for simplicity, chosen the 'Newtonian' ansatz with a simple threshold criterion, with yield stress σ_{1c}.

We solve the dynamical equations (12) and (13) numerically; details of the computation and the results obtained are provided in the next section.

3
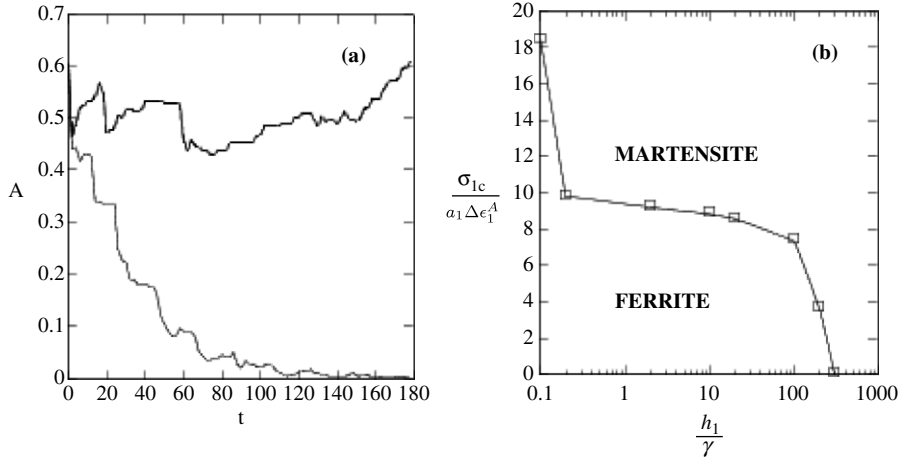
Figure 2. Results from the numerical solution of the dynamical equations in a 128×128 grid with a time step $\delta t = 0.002$. The parameters for this calculation are $a_1 = 100$, $a_2 = 1$, $a_3 = 0.01$, $\gamma = 5$. (a) Shape asphericity A of the growing nucleus as a function of time t from the elastoplastic model—bold line martensite and thin line ferrite. While the martensite nucleus remains eccentric, the ferrite nucleus becomes isotropic ($A \to 0$) at late times. (b) Dynamical phase diagram in the σ_{1c}–h_1 plane (expressed in units of $a_1 \Delta \epsilon_1^A$ and γ, respectively), starting from the same (elliptical) initial seed. The shape asphericity A at later times and the order parameter strain e_3 have been used to determine the phases.

4. Elastoplastic theory: numerics and results

4.1. Algorithm for solving dynamical equations

We have used a simple real space scheme to obtain the numerical solution of the partial differential equations (12) and (13). This involves discretizing over a lattice of square cells of size $\delta x = 1$. We have used 128×128 cells to obtain the phase diagram (figure 2) and 512×512 cells for figures 3–5. The initial value problem in time is solved using an Euler scheme with a time step of $\delta t = 0.002$ which is sufficient to avoid numerical instabilities. Below we give the sequence of steps involved in the iteration of the discretized equations.

Step 1. We start with initial values for e_3, its time derivative $\dot{e}_3$ and e_1^P defined over all the cells in our lattice and for time t. First, we need to compute the (slaved) affine strain ϵ_1^A from the OP strain e_3 by solving (10). The affine strain e_1^A together with the known e_1^P determines the total strain e_1 at t. In real space, (10) becomes

$$\nabla^2 e_1(x, y) = \rho_3(x, y, \{e_3\}). \quad (14)$$

Equation (14) is analogous to a Poisson equation for the 'charge density':

$$\rho_3(x, y, \{e_3\}) = q_{13} \frac{\partial^2}{\partial x \, \partial y} e_3(x, y) \quad (15)$$

and we need to solve it for the (Dirichlet) boundary condition $e_1 \to 0$ for $x, y \to \infty$. This is done by discretization in real space and by using an iterative scheme with a small over-relaxation and a convergence criterion of 1 in 10^6 [10]. For convenience in what follows, we refer to this solution using the notation $e_1 = \mathcal{P}(\{\rho_3\})$.

Our numerics can be checked for accuracy by comparing the results with those of simple choices for e_3 for which e_1^A (the

same as e_1) may be obtained analytically. For example, for e_3 which is nonzero only within a square of size $2a$, namely

$$e_3(x, y) = e_0 \Theta(a + x)\Theta(a - x)\Theta(a + y)\Theta(a - y), \quad (16)$$

($\Theta(x)$ is the Heaviside step function) e_1^A is the electrostatic potential for a set of four charges $+e_0$, $-e_0$, $+e_0$ and $-e_0$ at the vertices of a square (a, a), $(a, -a)$, $(-a, -a)$, $(-a, a)$ in two dimensions. This is given by

$$
e_1^A(x, y) = \frac{e_0}{2} \left[\ln \left(\frac{[(x - a)^2 + (y - a)^2]}{[(x + a)^2 + (y - a)^2]} \right. \right.
$$
$$
\left. \left. \times \frac{[(x + a)^2 + (y + a)^2]}{[(x - a)^2 + (y + a)^2]} \right) \right]. \quad (17)
$$

On the interfaces $y = \pm a$ and $x = \pm a$ it is easy to see that $e_1^A \sim \pm x$ (and $\pm y$, respectively) except near the corners where there are weak logarithmic singularities. Incidentally, this linear approximation for e_1^A is the same as the initial value of the density fluctuation $\phi(\mathbf{r}, 0)$ used in [11] and [8]. The presence of e_1^A modifies the interfacial energy of a rectangular nucleus of martensite of length L and width W containing N twins leading to the experimentally observed scaling law $L/N \sim W^{1/2}$ [11].

Our numerical result for e_1^A for the choice of e_3 given in (16) reproduces the analytic form (17) to within a few per cent.

Step 2. Knowing the strain e_1 at time t, we next update the plastic strain e_1^P to the next time step $t + \delta t$ by iterating (13). For this, the local stress $\sigma_1 = a_1 e_1$ (plus any external stress if present) is obtained for all the cells and is then used as input to (13).

Step 3. Lastly, we have to update e_3 and $\dot{e}_3$ for which one needs to compute the functional derivative

$$\frac{\delta \mathcal{F}}{\delta e_3} = \frac{\delta \mathcal{F}_3}{\delta e_3} + \frac{\delta \mathcal{F}_1}{\delta e_3} \quad (18)$$

4
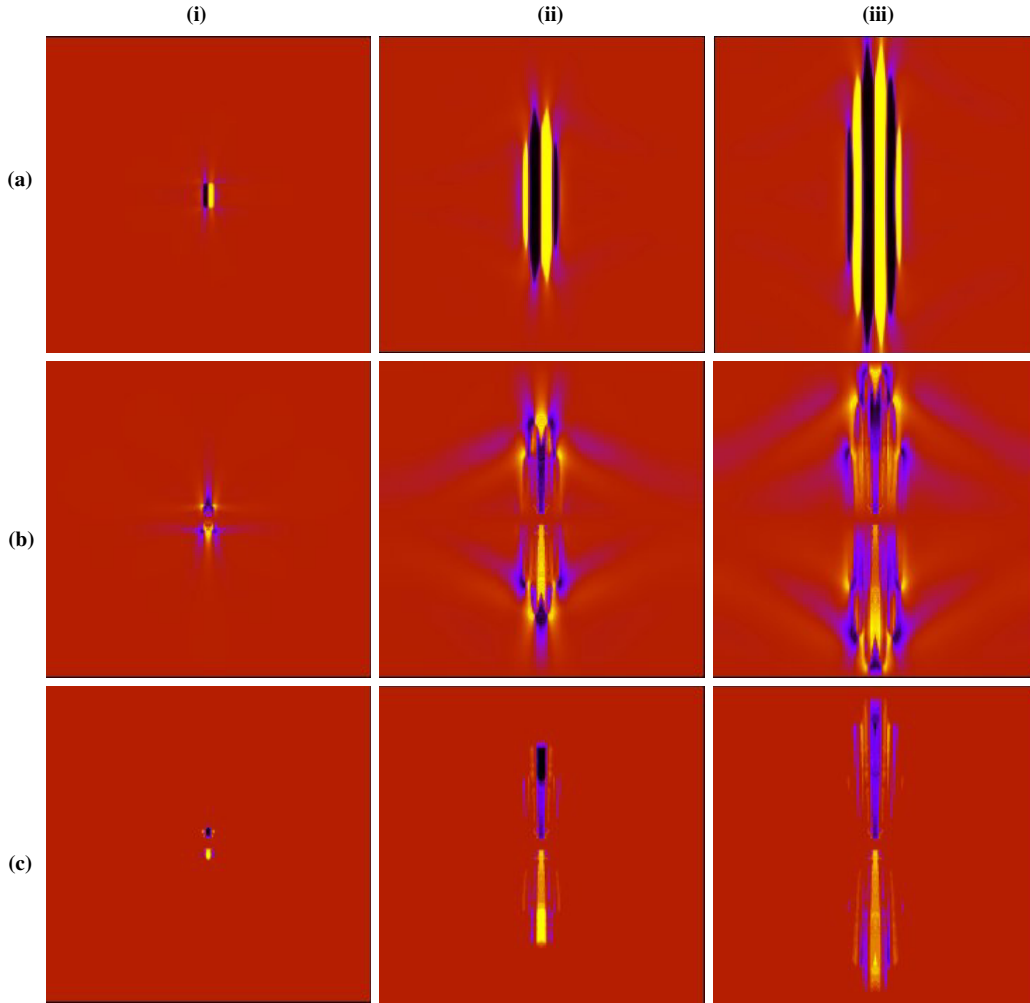
Figure 3. Time development of the affine strain, stress and non-affine strain following a quench into the martensite phase for 512×512 cells at (i) $t = 30$, (ii) $t = 600$ and (iii) $t = 800$, starting from an initial elliptical nucleus with a single twin boundary. The plasticity parameters $|\sigma_{1c}| = 1$ and $h_1 = 1$ while the rest of the parameters are as before. (a) Profile of affine OP strain e_3, showing the initial growth parallel to the twin interface, followed by the dynamical addition of twins. Colors: yellow (white in the print edition) to black maps the range $-1 < e_3 < 1$. Brown (gray in the print edition) region denotes retained austenite, $e_3 = 0$. (b) Corresponding profile of the local stress σ_1. The local stress is concentrated at the tips of the growing front where it approaches the threshold value σ_{1c} (i) and (ii). In the interior of the growing nucleus σ_1 relaxes to zero. Subsequently in (iii), the local stress gets large in regions where the new twins are being accommodated. Note the variation in the signs of the stress in the direction along which new twins are added. Colors: yellow (white in the print edition) to black maps the range $-1 < \sigma_1 < 1$. (c) Corresponding non-affine strain e_1^P, showing the initial advection by the transformation front, and its dynamical emergence as subsequent twins are added. e_1^P appears in regions where $\sigma_1 \sim \sigma_{1c}$ and $\sigma_1 \sim -\sigma_{1c}$. Colors: yellow (white in the print edition) to black maps the range $-0.01 < e_1^P < 0.01$.

where the two terms on the right-hand side represent functional derivatives of the parts of the free energy (7) involving only e_3 and e_1, respectively. The first term is straightforward and is given by

$$\frac{\delta \mathcal{F}_3}{\delta e_3} = -\nabla^2 e_3 + e_3 - 4(e_3)^3 + 6(e_3)^5, \qquad (19)$$

while the second term, after some algebra, can be shown to be

$$\frac{\delta \mathcal{F}_1}{\delta e_3} = a_1 \mathcal{P}(\{\rho_1\}) - c_1 \rho_1 \qquad (20)$$

where

$$\rho_1(x, y, \{e_3\}) = q_{13} \frac{\partial^2}{\partial x \, \partial y} e_1(x, y). \qquad (21)$$

Note that (21) involves the total e_1 which includes both affine as well as the non-affine strain. Even if $e_3 = 0$ to begin with, at subsequent times e_3 may be created due to the presence of nonzero e_1^P. One encounters such a situation during the heterogeneous nucleation of martensite near defect sites [12, 6] with pre-existing e_1^P. Secondly, the resulting form for the functional derivatives are highly non-local since they involve repeated solutions of the Poisson equation. However, if e_1^P is large the total NOP strain e_1 vanishes and the non-local coupling between spatially separated regions of the OP e_3 disappears.

4.2. Results: dynamical phase diagram

The most convenient comparison with the MD simulations of [1] is made by following the dynamics upon seeding the
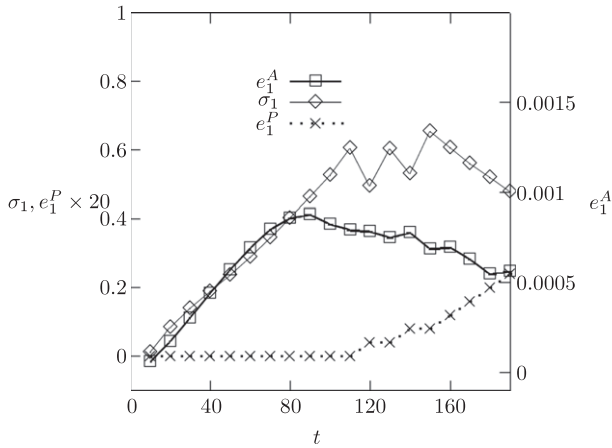
Figure 4. Evolution of the local affine strain e_1^A (scale on right), the local stress σ_1 and the non-affine part of the strain e_1^P for a cell $\Omega = (128, 100)$ on the twin axis following the quench into the martensite phase shown in figure 3. Note the initial linear regime, when $\sigma_1 \propto e_1^A$ and $e_1^P = 0$, followed by oscillations in σ_1 and the creation of e_1^P as the stress σ_1 rises to the threshold value $\sigma_{1c} = 1$. The resemblance to figure 8 from our MD simulations [1] is quite apparent. We have multiplied e_1^P by 20 in order to make it visible.

metastable square solid with a tiny elliptical, twinned nucleus. These calculations do not involve any imposed randomness or noise. We shall discuss the effects of quenched noise in the next section.

As in the MD simulation, we first obtain a dynamical phase diagram demarcating the regions where a martensite or ferrite is obtained upon quenching. This is done by studying the shape of the nucleus, in terms of the shape asphericity A defined before and twinning of the microstructure, in terms of the affine OP strain e_3. We focus on a special cut in

parameter space; we fix the coefficients appearing in (7) and γ, and explore the dynamical phase diagram in the plasticity variables, σ_{1c}–h_1 plane (figure 2(b)). The threshold stress σ_{1c} is expressed in units of $a_1 \Delta \epsilon_1^A$ (the affine stress at the structural transition), and h_1 in units of ℓ^2/γ (where ℓ, the thickness of the twin interface, has been taken to be 1). In figure 2(a), we plot A as a function of time for an anisotropic (twinned) nucleus and an isotropic (untwinned) nucleus; the value of A at late times (figure 2(a)) and the profile of the order parameter strain are used to map out a dynamical phase diagram containing the martensite and ferrite, figure 2(b).

We discuss several novel features of this dynamical phase diagram. For instance, even when the threshold stress σ_{1c} is zero, a martensite can form if the plasticity relaxation rate is small (large h_1) compared to the rate of growth of the nucleus. This feature was already present in our earlier calculation [8], where the dynamics of the local density fluctuations determined the selection of microstructure and is an inescapable feature of real martensites [13]. The phase diagram, figure 2(b), is constructed for a fixed value of under-cooling. As the degree of under-cooling changes, this phase boundary changes slightly, but not a whole lot—the ferrite being favored for low under-cooling. More significantly, the plasticity relaxation time h_1 increases with the lowering of temperature. Thus, by starting out in the ferrite phase, one can cross the phase boundary into the martensite by simply lowering the temperature, identified as the martensite start or M_s temperature. In addition, there is a well-defined plateau yield stress over three decades in h_1, suggesting that the yield stress is independent of temperature over this range. This is consistent with our MD simulations. Finally, it must be noted that the dynamical phase diagram figure 2(b) is constructed from the nature of the first critical nucleus that forms. In a macroscopic sample, a ferrite nucleus may eventually nucleate
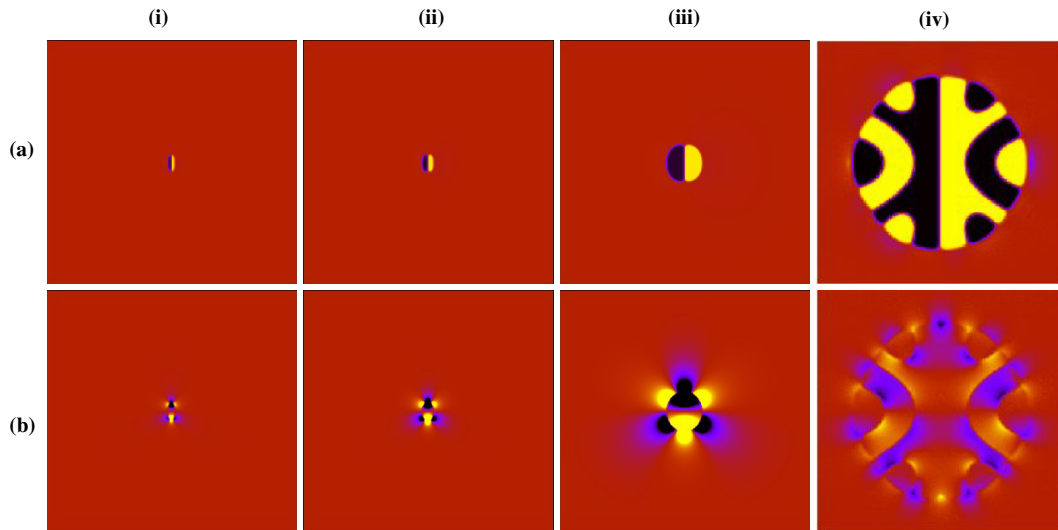
Figure 5. Time development of the affine and non-affine strain following a quench into the ferrite phase, at (i) $t = 40$, (ii) $t = 200$ and (iii) $t = 1000$, starting from an initial elliptical nucleus with a single twin boundary. The plasticity parameters $\sigma_{1c} = 10^{-4}$ and $h_1 = 1$, while $a_3 = 0.1$; the rest of the parameters are as before. (a) Profile of affine OP strain e_3, which shows the initial elliptical nucleus growing approximately isotropically. Colors: yellow (white in the print edition) to black maps the range $-1 < e_3 < 1$. (b) Corresponding non-affine strain e_1^P, showing its invasion into the 'bulk' of the growing polycrystalline nucleus. Colors: yellow (white in the print edition) to black maps the range $-0.01 < e_1^P < 0.01$. (iv) (a) and (b) show e_3 and e_1^P, respectively, for a very late time ($t = 1600$) ferrite nucleus in a 256×256 system with parameters $a_3 = 0.01$, $h_1 = 0.1$ and $\sigma_{1c} = 0$. The stress σ_1 is negligibly small for all (i)–(iv).

and grow *even in the martensite phase*, once the plastic strain e_1^P gets enough time to relax. This is consistent with our MD simulations and agrees with results of isothermal quenching experiments in real materials [14].

Having displayed the dynamical phase diagram we can perform quenches to the martensite and ferrite phase, and study the time development of the profiles of e_3, σ_1 and e_1^P (figures 3 and 5). Using plasticity parameters corresponding to the martensite phase, figure 3 shows the temporal evolution of a twinned nucleus, in perfect analogy with our MD simulations. The nucleus initially grows parallel to the twin boundary (figure 3(i)), while the stress σ_1 approaches the threshold at the growing tips. As a result the plastic strain e_1^P gets to be large at these tips. As the nucleus grows, these highly stressed and plastic regions are advected by the growing tips. In the interior transformed region, the stress relaxes to a sub-threshold value and the plastic deformation goes to zero. The sequence of events exactly mimic the dynamics of the ϵ_V^A, χ and NAZs of figure 4 of [1]. To study the time evolution of the NAZs in more detail, we focus on a single cell, Ω, midway within our computation box, along (but not on) the twin boundary of the initial seed within the untransformed square lattice. With time, the growing tip of the nucleus approaches, and then sweeps by, Ω, in the process transforming it into the triangular phase. This situation is analogous to that shown in figure 8 from our MD simulations [1]. We plot the local e_1, σ_1 and e_1^P at Ω as a function of time t in figure 4. As in figure 8 of [1], initially Ω, which lies ahead of the approaching transformation front, begins to deform elastically due to stress generated at the growing tip. The resulting volumetric strain e_1 is proportional to the local σ_1 and $e_1^P = 0$. As the tip of the growing nucleus approaches Ω, σ_1 rises and tends to cross the threshold, σ_{1c}. At this instant, e_1^P begins to form, reducing σ_1 to a value below σ_{1c}. As the nucleus grows further, σ_1 within Ω increases again—and the process repeats, producing a local stress which oscillates rapidly in time. These oscillations result from cooperative jamming and unjamming events caused by alternating build-up of σ_1 due to interface motion and its relaxation by creation of NAZs [15]. The region of high (and oscillating) local stress and the NAZ travels with the growing tip, being advected by the moving transformation front. The strong resemblance between figure 8 of [1] and figure 4 is striking. Eventually, the interface crosses Ω and σ_1, as well as e_1^P, relaxes to zero within the bulk of the product phase.

The subsequent dynamics, figure 3(iii), goes beyond the timescales accessed in the MD simulation. The dynamics now proceeds perpendicular to the twin interface, adding new twins (symmetrically disposed) as time proceeds. The production of new twins with a fixed width is a consequence of the anisotropic, non-local interactions connecting spatially separated regions with nonzero e_3.

Note that the affine NOP strain mediates the anisotropic, long-ranged interactions [2]; the presence of the plastic NOP strain *screens* this interaction, making it short range. The emergence of the OP strain in the form of twins leads to an increase in the local stress σ_1, which in turn generates plastic flow on crossing the threshold (figure 3(c)). The plastic strain, once produced, reduces the value of the total NOP strain and,

therefore, that of the non-local interaction. In the case of the martensite, this reduction is not complete. The stress σ_1 decreases to zero in the interior of the martensitic nucleus, so that any given region undergoes the same sequence of transformations: untransformed → elastic distortion → non-affine → transformed. This temporal sequence is also seen in our MD simulations.

We now use plasticity parameters corresponding to the ferrite phase; figure 5 depicts the time evolution of an isotropic, polycrystalline ferrite nucleus, starting from the same initial conditions as above. For small values of σ_{1c}, the plastic strain e_1^P is produced readily, and on average largely cancels out the effect of the affine NOP strain. This significantly reduces the magnitude and range of the non-local interactions, which were responsible for producing the twins. The local stress σ_1 tends to cross the threshold (positive and negative) in the *interior* of the growing nucleus, which leads to an *invasion* of the non-affine strain e_1^P into the 'bulk' of the isotropically growing, polycrystalline nucleus. This results in incoherent grain boundaries in the interior of the growing nucleus. Note that the symmetry of the pattern, figure 5, arises because the evolution equations are deterministic; any noise would destroy this symmetry and make the grain boundaries rough and orient randomly. The sequence of events then exactly mimic the dynamics of the ϵ_V^A, χ and NAZs of figure 5 of [1].

We believe we have successfully constructed a general elastoplastic description for the dynamics of solid state transformations, which is capable of describing different microstructures and addresses the issues of microstructure selection. The qualitative picture that emerges from the elastoplastic model closely resembles our MD simulation results (Part I). In the next section, we will present a discussion and some implications of our elastoplastic theory.

5. Discussion

By constructing a theory for microstructure selection, we successfully bridge two apparently disparate descriptions of the dynamics of ferrites and martensites within a unified framework. This has been achieved at the cost of enlarging the space of dynamical variables to include non-affine deformations. Have we lost some of the special features of martensites in the process? What implications does our description of solid state nucleation and microstructure selection have for conventional nucleation theory?

(i) *Unified description of martensite and ferrite*: Strain-only theories [2] set $\epsilon_V^P = 0$ and use (3) and (6) to eliminate ϵ_V^A in terms of ϵ_T^A, leading to long-ranged interactions and dissipation in ϵ_T^A, both of which are spatially anisotropic. This is ultimately responsible for producing the twinned microstructure of martensites in the strain-only description; the size of the twins is set by elastic parameters alone [2]. These theories cannot describe the occurrence of the ferrite. In our elastoplastic description, inclusion of local plastic deformation in the form of ϵ_V^P has two effects—it *screens* and *isotropizes* the non-local interaction and dissipation kernel. This
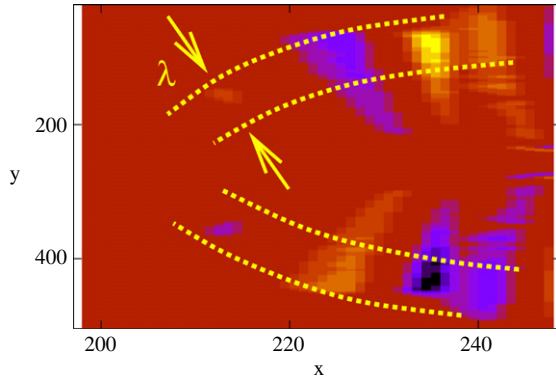
Figure 6. Close-up of a plot of the plastic strain e_1^P for a growing martensite at $t = 800$ (same as in figure 3(c)(iii)). Note the presence of NAZs with alternating signs of e_1^P accompanying the growing martensite phase—see the region within the dashed lines. This figure needs to be compared with figure 1 of [1]. When the strain fields are coarse-grained over the length scale λ the contribution from these alternating patches cancel and full elastic compatibility is restored.

is ultimately responsible for the destruction of the twin pattern, resulting in a ferrite. Further, in contrast to strain-only theories, the size of the twins depends on elastic, as well as plastic, parameters. We provide a detailed analysis of these effects in a forthcoming publication.

(ii) *Emergence of average compatibility from the elastoplastic dynamics*: Our elastoplastic theory provides an understanding of how the strict local compatibility of strain-only theories [2, 16] can be reconciled with the average compatibility of geometrical theories [17] when describing the dynamics of the martensite. We find that, in the regime where the martensite obtains, our dynamical equations reduce to the equations of the strain-only theories, when we coarse-grain over a scale λ corresponding to the size of the NAZs. Simultaneously, the equations of constraint, namely the modified St. Venant's condition (8), reduces to the usual St. Venant's elastic compatibility, provided we coarse-grain over the same scale λ. This can be seen by explicitly writing out (8):

$$\nabla^2 e_1^A - (\nabla_x^2 - \nabla_y^2)e_2 - 4\nabla_x\nabla_y e_3 = \nabla^2 e_1^P.$$

In figure 6, we have re-plotted e_1^P for time $t = 800$ (figure 3(c)(iii)) in order to show the NAZs in detail. Remarkably, the martensite plates are accompanied by patches where $e_1^P \neq 0$ and alternate in sign. If the system is coarse-grained over a distance λ the effect of these patches cancel and we recover the usual elastic compatibility condition. This emergence of compatibility upon coarse-graining over the scale of the plastic zone was noted in [11]. As the critical stress σ_{1c} increases, the size of the NAZs decreases and so does the coarse-graining length scale λ. Note that the coarse-graining appropriate for the emergence of the usual elastic compatibility does not wash out the twinned microstructure of the martensite; the 'phase' of the averaging is so as to produce a planar martensite–austenite interface as shown in figure 1 of [1].

(iii) *Reversibility of martensitic transformations*: How do we reconcile the inevitable creation and evolution of plasticity in the form of NAZs with the apparent reversibility of martensitic transformations, as observed in shape-memory alloys? Here we provide some preliminary comments, which has been taken up in greater detail elsewhere [18]. In essence, microstructural reversibility in martensites is related to the nature of the accompanying plastic deformation. The key feature of plastic deformation in the NAZs is that it is largely associated with the NOP sector, which in turn is *slaved* to the transformation strain. Indeed, even the slightest amount of plasticity in the OP sector would make the transformation irreversible. This is apparent in martensites involving Fe alloys, which do not exhibit shape-memory[4]. Within our own model system, a deep quench to the $\alpha = 0$, $v_3 = 0$ region produces a *triangular* solid which is not related to the parent square lattice by a group–subgroup relation [9]. During the reverse transformation, therefore, there is no unique parent lattice that the system can revert to. This produces non-affineness in the OP sector due to a multiplicity of affine paths and destroys reversibility.

The other relevant feature exhibited by the NAZs associated with martensites is the special nature of the particle trajectories [8, 1]. Particles in the NAZs formed during martensitic growth move ballistically and in a coordinated manner. It is these two properties of the NAZs discussed here that ultimately renders the square to rhombus martensitic transformation reversible, in spite of significant transient and localized plastic deformation.

(iv) *Inconsistency with Ostwald's step rule*: Ostwald's step rule of 1897 states that *'the phase that nucleates need not be the stable phase, but the one that is closest in free energy to the parent phase... '*. This rule has been interpreted by Stranski and Totomanov [20] to mean that the phase which has the lowest free-energy barrier is nucleated. While it is easy to appreciate the applicability of this rule for phase transformations in simple systems having a uniquely defined barrier crossing event along the path of the transformation, it is more difficult to apply such considerations to, say, atomic rearrangements and the generation of NAZs where many barriers with different attempt frequencies may be involved [21]. As discussed in section 3, the selection of microstructure depends both on parameters in the free-energy functional (7) and dynamical parameters in (12) and (13). This is explicitly shown in figure 2, where the microstructure depends on the plasticity dynamics, in terms of the yield stress σ_{Vc} and viscosity h.

(v) *Randomness and heterogeneous nucleation at defect sites*: The results presented in section 4, were obtained with initial conditions corresponding to a *small elliptical nucleus* and the choice of dynamical parameters corresponding to martensitic and ferritic growth. An alternate initial condition for the nucleation dynamics is to prescribe a spatially random stress profile, e.g. a random

---

[4] Finally, this question, and consequently reversibility, is determined by the symmetry of the OP strains, see, for example, [19].
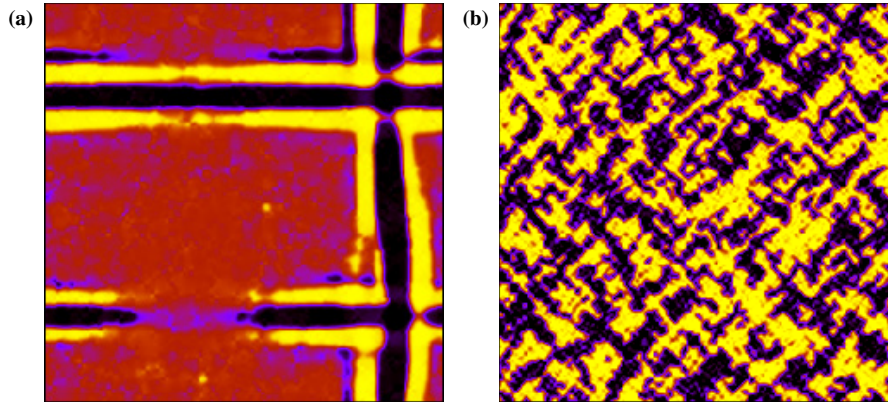
Figure 7. Plot of the OP strain e_3 for time $t = 1000$ for a martensite (a) with $\sigma_{1c}/a_1\Delta e_1 = 2500$ and for a ferrite (b) with $\sigma_{1c} = 0$; $h_1/\gamma = 0.1$ for (a) and (b). The color scheme is as in figure 3(a). In both these calculations, a quenched, Gaussian, random stress $\sigma_1(\mathbf{r}, t)$ with zero mean and variance $S_1 = 10$ was used to nucleate the product phase. Note that quenched randomness does not affect the overall characteristics of the martensite at late times. The ferrite grains, however, become much smaller with grain boundaries which are broad compared to the size of the grains.

σ_1'. In real materials, this would correspond to frozen-in defect structures. This quenched random stress would add to the internal stress so that the total stress $\sigma_1 = a_1(e_1 + e_1^P) + \sigma_1'$. The *initial* stages of the dynamics of nucleation and growth are sensitive to the initial distribution, which we take from a Gaussian distribution with zero mean and width S_1.

For instance, if $S_1 \ll \sigma_{1c}$, the threshold, inhomogeneous elastic strains in e_1 develop which initiate nucleation of the product via its coupling to e_3. As the dynamics proceeds, local (total) σ_1 gets enhanced at the transformation fronts, giving rise to plastic deformations. On the other hand, if $S_1 > \sigma_{1c}$, the threshold, then local regions can develop appreciable plastic strains, equation (13). The elastic coupling between e_1^P and e_3 through the functional derivative in equation (12) then causes the nucleation of the product phase. The lag time for nucleation is appreciably faster compared to when $S_1 \ll \sigma_{1c}$. The qualitative features of the phase diagram, figure 2, are unaltered by the presence of quenched random stress fields, though it 'enlarges' the regime over which the ferrite phase obtains. Figure 7 shows that the ferrite microstructure is altered; the grain sizes shrink and the grain boundaries thicken with increased randomness. The martensite microstructure, at the scale of the twin pattern, is, however, unaltered, though again the distribution of martensitic grains gets smaller with increased disorder. This robustness of martensitic patterning over the scale of the twins is significant and we wish to revisit this aspect in a detailed study. We may mention here that there has been several detailed studies of heterogeneous nucleation and the possibility of spinodal-like ordering for the freezing transition [22]. We plan to undertake similar studies in the future for our system, especially for the case when the jump in the order parameter during the transition becomes small.

(vi) *Dynamical phase diagram and TTT curves*: The dynamics of microstructure selection is conventionally represented by a time–temperature–transformation (TTT) diagram, constructed in the form of contour plots of the proportion of each constituent (martensite or ferrite) as a function of time during an isothermal transformation at different quench temperatures [14, 12]. Figure 2 is the dynamical phase diagram computed within our elastoplastic theory; this can be converted to the typical TTT curve, provided we know the temperature dependence of σ_{1c} and h_1. Such a temperature dependence may be put in phenomenologically, as in figure 4 of [8], or obtained from a first-principles non-affine field theory.

(vii) *Future work*: It should be possible to extend our elasto-plastic theory to include the effects of impurities such as interstitial carbon in Fe (as in steel) [23], which undergoes significant non-affine deformation [14]. Interstitial carbon, represented by a diffusive concentration field ψ, would enter into both the dynamical equations for the affine and non-affine strains. Thus any attempt to understand microstructure selection in systems such as steel would involve the study of the coupled dynamics of the affine strain, non-affine strain and concentration field ψ.

Finally, apart from restoring the full tensorial character of the elastoplastic description, we need to explore in greater detail the consequences of general thresholding and yield flow in the plasticity dynamics accompanying solid state transformations. In a later paper, we will discuss the dynamical response of the transforming solid to time-dependent external stresses (or strains), and periodic quenches across the phase boundary.

References

[1] Bhattacharya J, Paul A, Sengupta S and Rao M 2008
J. Phys.: Condens. Matter **20** 365210
[2] Barsch G R *et al* 1987 *Phys. Rev. Lett.* **59** 1251
Rasmussen K Ø *et al* 2001 *Phys. Rev. Lett.* **87** 055704
Lookman T *et al* 2003 *Phys. Rev.* B **67** 024114 and references
therein
[3] Landau L D and Lifshitz E M 1986 *Theory of Elasticity*
(Oxford: Pergamon)
[4] Lubarda V A 2002 *Elastoplastic Theory* (Boca Raton, FL: CRC
Press)
[5] Langer J S 2008 *Phys. Rev.* E **77** 021502
[6] Phillips R 2001 *Crystals, Defects and Microstructures:
Modeling Across Scales* (Cambridge: Cambridge University
Press)
[7] Zippelius A, Halperin B I and Nelson D R 1980 *Phys. Rev.* B
22 2514
[8] Rao M and Sengupta S 2003 *Phys. Rev. Lett.* **91** 045502
[9] Hatch D M, Lookman T, Saxena A and Shenoy S R 2003 *Phys.
Rev.* B **68** 104105
[10] Abramovitz M and Stegun I A 1972 *Handbook of
Mathematical Functions* (New York: Dover)
Press W H, Teukolsky S A, Vetterling W T and Flannery B P
1992 *Numerical Recipes: The Art of Scientific Computing*
(Cambridge: Cambridge University Press)
[11] Rao M and Sengupta S 1997 *Phys. Rev. Lett.* **78** 2168
Rao M and Sengupta S 1999 *Curr. Sci.* **77** 382
Sengupta S and Rao M 2003 *Physica (Amsterdam)* A
318 251
[12] Cahn R W and Haasen J 1996 *Physical Metallurgy* 4th edn
(Amsterdam: Elsevier)
Kachaturyan A G 1983 *Theory of Structural Transformations in
Solids* (New York: Wiley)
[13] Bhadeshia H K D H, private communication
[14] Bhadeshia H K D H 1992 *Bainite in Steels* (London: Institute
of Materials)
[15] Liu A J and Nagel S R 1998 *Nature* **396** 21
[16] Ahluwalia R and Ananthakrishna G 2001 *Phys. Rev. Lett.*
86 4076
Sreekala S and Ananthakrishna G 2003 *Phys. Rev. Lett.*
90 135501
Sreekala S, Ahluwalia R and Ananthakrishna G 2004 *Phys.
Rev.* B **70** 224105
[17] Ball J M and James R D 1992 *Phil. Trans. R. Soc.* A **338** 389
Bhattacharyya K *(unpublished notes)* available from http://
mechmat.caltech.edu/ Olson G B and Owen W S (ed) 1992
Martensite (Ohio: ASM International, The Materials
Information Society)
[18] Bhattacharya J, Sengupta S and Rao M 2008 *J. Stat. Mech.*
P06003
[19] Bhattacharya K, Conti S, Zanzotto G and Zimmer J 2004
Nature **428** 55
[20] Ostwald W 1897 *Z. Phys. Chem.* **22** 289
Stranski I N and Totomanov D 1933 *Z. Phys. Chem.* **163** 399
[21] ten Wolde P R and Frenkel D 1997 *Science* **277** 1975
[22] Trudu F, Donadio D and Parrinello M 2006 *Phys. Rev. Lett.*
97 105701
Wang H, Gould H and Klein W 2007 *Phys. Rev.* E **76** 031604
[23] Bouville M and Ahluwalia R 2006 *Phys. Rev. Lett.* **97** 055701